



Inverse heat transfer approach for IR image reconstruction: Application to thermal non-destructive evaluation

Fernando López Rodríguez*, Vicente de Paulo Nicolau

Mechanical Engineering Department, Federal University of Santa Catarina, 88040-900, Florianópolis, Santa Catarina, Brazil

ARTICLE INFO

Article history:

Received 4 May 2011

Accepted 12 September 2011

Available online 21 September 2011

Keywords:

Thermal non-destructive test

Thermal simulation

Inverse heat transfer

Infrared thermography

ABSTRACT

An inverse heat transfer method is developed to characterize subsurface defects in ceramic materials through the reconstruction of the IR image obtained by numerical simulation. This study focuses on the application of the Conjugate Gradient Method (CGM) of minimization for the determination of the thermal conductivity and the depths of defects present in ceramic materials. To this aim, an inspection method which consists of imposing a transient regime process in the sample test is proposed, starting from an elevated and uniform temperature and applying a cooling process over the time. Surface thermal images are collected during the cooling process using an infrared camera. A mathematical model based on the transient behavior of the ceramic sample during the inspection is proposed to study the different heat transfer mechanisms and detectability levels of the simulated defects. The numerical solution of the model was developed using the Finite Volume Method (FVM), in which the approximated equations are obtained by performing energy balances for each elementary volumes. Experimental and simulated temperature decay curves of defective areas are used to determine the properties of the above-mentioned defects.

© 2011 Elsevier Ltd. All rights reserved.

1. Introduction

The need to improve production quality has led to the development of methods and techniques that, supported by advances in computing and material sciences, allow the presence of internal irregularities in materials to be detected without affecting their physical integrity and subsequent service. These evaluation methods are known as Non-Destructive Tests (NDT). Among the different NDT methods employed nowadays, infrared thermography (IRT) represents one of the most promising techniques for the inspection of materials and structures using the principle that all bodies with a temperature above 0 K emit infrared radiation. Through the measurement of this emitted radiation, IRT allows the detection and characterization of internal defects by analyzing alterations or contrasts in the thermal pattern of the material surface.

IRT as an NDT technique is divided in two broad groups: passive and active thermography. Passive thermography, based on a qualitative analysis, is deployed without external stimulation to provoke gradients in the thermal pattern of the inspected surface. In active

thermography, external stimulation of the material is induced to produce an internal heat flux. Subsurface defects will affect the heat diffusion rate, producing a thermal contrast on the surface being tested. Detailed information concerning these passive and active approaches can be found in [1].

The detection efficiency of such techniques has increased mainly because of improved performance of the equipment and the contribution provided by computers (hardware and software), however, defect characterization procedures still represent a broad field of study. In this regard, inverse heat transfer approaches constitute reliable techniques to determine parameters associated with the detected defects, especially when dealing with infrared images. Studies from Magnani and Tavares da Silva [2], Barreira and de Freitas [3] and Guerrero et al. [4] have demonstrated the successful use of infrared thermal images in evaluating and determining the thermophysical properties of materials.

In quantitative infrared thermography inspections, two important parameters to be determined are the thermal conductivity and the depth of the defects present in the material. Following the inverse heat transfer approaches for characterization purposes, it is important to highlight contributions from Sawaf and Ozisik [5] and Huang and Yan [6] who investigated the application of the inverse problem in determining temperature-dependent thermal conductivity and heat capacity by using a thermal model based on the one-dimensional transient heat conduction equation. Huang and Chin

* Corresponding author. Tel.: +55 48 3234 4615; fax: +55 48 3721 761.

E-mail addresses: flopez@cwpanama.net (F.L. Rodríguez), vicente@emc.ufsc.br (V. de Paulo Nicolau).

Nomenclature		β	thermal expansion coefficient (K^{-1})
A	area (m^2)	γ	conjugation coefficient
cp	specific heat ($J/kg\ K$)	ε	emissivity – tolerance
D	direction of descent	ν	momentum diffusivity (m^2/s)
h	convection heat transfer coefficient ($W/m^2\ K$)	ρ	density (kg/m^3)
H	height (m)	σ	Stefan-Boltzmann constant $W/(m^2\ K^4)$
J	objective function	Ω	spatial direction
k	thermal conductivity ($W/m\ K$)	Subscripts	
L	length (m)	<i>amb</i>	ambient
N_x, N_y, N_z	numbers of elements in x, y and z coordinates	<i>conv</i>	convection
P	perimeter (m)	<i>i j, k</i>	grind points
t	time (s)	<i>lat</i>	lateral
T	temperature (K)	<i>low</i>	lower
T_s	simulated temperature (K)	<i>o</i>	initial
W	width (m)	<i>s</i>	surface
x, y, z	Cartesian coordinates	<i>sup</i>	superior
Y_m	experimental temperature (K)	<i>upper</i>	upper
y	depth (m)	Superscripts	
Greek symbols		p	time step (s), iterative level
α	thermal diffusivity (m^2/s)		

[7] investigated the application of the conjugate gradient method (CGM) of minimization for the imaging of the unknown thermal conductivity of a non-homogeneous material. Another study with important features similar to those presented herein was carried out by Chand and Cheng [8] who applied a non-destructive inverse method in the determination of irregular distributions in proton exchange membrane fuel cells (PEMFCs) using the steady-state 3D energy equation.

The present study investigates the application of the inverse heat transfer problem to characterize thermal conductivity and the depth of hidden defects in ceramic materials using the active thermography approach. For this purpose a mathematical model based on the 3-D transient heat equation is proposed to describe the thermal behavior of the sample when exposed to a cooling process at ambient temperature. The thermal losses by convection and radiation during the inspection by IRT are also considered in the model. The detectability level as a function of the initial cooling temperature is studied as well as the thermal behavior of the defective area when varying the defect depth.

The inverse problem for the estimation of the thermal conductivity and depth of hidden defects is solved by the CGM of minimization as described by Hanke [9]. This method is used to evaluate the gradients of the objective function and to find the conjugate directions for the updated solutions with the help of a numerical sensitivity analysis as proposed by Cheng and Wu [10]. In general terms, in a reasonable number of iterations the convergence can be attained.

2. Direct formulation

2.1. The proposed thermal NTD model

The thermal model proposed herein and used to predict the heat transfer during a non-destructive test by IRT, consists of imposing a transient regime process on a ceramic sample (with dimensions $W=100\text{ mm} \times L=215\text{ mm} \times H=45\text{ mm}$), starting from an elevated and uniform temperature, and then applying a cooling process over time. During the imposed cooling process, the sample surface is monitored using an infrared camera, as it's shown in Fig. (1):

At the beginning of the IR inspection the sample has a higher temperature with respect to its surrounding, leading to transfer heat by conduction within the material and by convection and radiation between its surface and the external environment. The solution of the 3-D transient heat conduction equation provides the temperature evolution field of the surface being inspected, described by:

$$\rho cp \frac{\partial T}{\partial t} = \nabla \cdot (k \nabla x) \quad (1)$$

The initial condition is defined by Eq. (2):

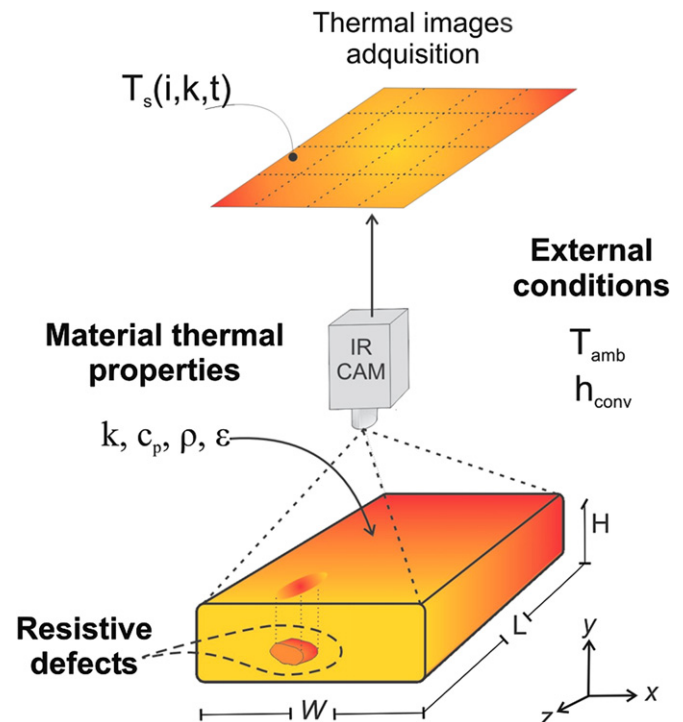


Fig. 1. Thermal Model for NDT by Infrared Thermography.

$$T(x, y, z)_{t=0} = T_0 \quad (2)$$

The boundary conditions, including the heat transfer by convection and radiation between all the sample surfaces and the environment is defined by Eq. (3):

$$n \cdot (k \nabla T) = h_{conv}(T_{amb} - T) + \sigma \varepsilon (T_{amb}^4 - T^4) \quad (3)$$

In Eqs. (1) and (3), T represents the temperature of the material along coordinates x , y and z ; T_{amb} is the ambient temperature, considering that the air and the external environment are at the same temperature. The surface emissivity is represented by ε and σ is the Stefan–Boltzmann constant. The material thermal conductivity is given by k while the specific heat and the density are c_p and ρ , respectively. The convection heat transfer is given by h_{conv} and t represents the variable time. Through the solution of Eq. (1) using the initial condition given by Eq. (2) and the boundary conditions given by Eq. (3), is possible to determine the thermal map T_s of the sample surface, which is equivalent to the thermogram sequence obtained using an infrared camera during the NDT.

2.2. Numerical solution approach

Numerical solution methods constitute important tools for the study of complex phenomena described by higher-order differential equations. In this study the Finite Volume Method (FVM) was used as a numerical solver. This method consists of the integration of space and time, over an elemental volume, the energy equation in the conservative form, which is equivalent to performing energy balances over all of the elemental volumes [11]. Fig. (2) shows an energy balance over a generic elemental volume with dimensions $dx \times dy \times dz$, which is the methodology used to obtain all the local equations of temperature. The quantities q_x , q_y , and q_z represent the incoming and outgoing heat fluxes to the volume control, considering any of the three heat transfer process: conduction, convection and radiation.

The domain under study was divided into twenty-seven (27) types of elemental volume, according to the position and the heat transferred to the external environment and its neighborhoods. As shown in Fig. (2), the energy balance provides the local temperature equation at the center of the volume (cell-center mesh), while

the material thermal properties (thermal conductivity, density and specific heat) remain stored at the interface of the control volume.

Integrating Eq. (1) over the control volume shown in Fig. (2),

$$\int_t \int_\Omega \rho c_p \frac{\partial T}{\partial t} = \int_t \int_\Omega \nabla \cdot (k \nabla T) \quad (4)$$

is obtained the discrete energy balance for internal volumes given by:

$$\begin{aligned} \frac{\rho c_p \Delta x \Delta y \Delta z}{\Delta t} (T_{(i,j,k)}^{p+1} - T_{(i,j,k)}^p) &= \frac{k}{\Delta x} (T_{(i-1,j,k)}^p - T_{(i,j,k)}^p) \Delta y \Delta z \\ &+ \frac{k}{\Delta x} (T_{(i+1,j,k)}^p - T_{(i,j,k)}^p) \Delta y \Delta z \\ &+ \frac{k}{\Delta y} (T_{(i,j-1,k)}^p - T_{(i,j,k)}^p) \Delta x \Delta z \\ &+ \frac{k}{\Delta y} (T_{(i,j+1,k)}^p - T_{(i,j,k)}^p) \Delta x \Delta z \\ &+ \frac{k}{\Delta z} (T_{(i,j,k-1)}^p - T_{(i,j,k)}^p) \Delta x \Delta y \\ &+ \frac{k}{\Delta z} (T_{(i,j,k+1)}^p - T_{(i,j,k)}^p) \Delta x \Delta y \end{aligned} \quad (5)$$

In Eq. (5), the first term corresponds to the transient (or thermal inertia) term, followed by the incoming and outgoing conduction heat fluxes in each of the spatial coordinates. Due to the diffusive nature of the internal heat conduction process within the sample test, the derivatives present in the energy equation were approximated using central difference scheme. Likewise, the explicit formulation was used as the temporal interpolation function.

Similarly, integrating Eq. (3) over space and time,

$$\int_t \int_\Omega n \cdot (k \nabla T) = \int_t \int_\Omega h_{conv}(T_{amb} - T) + \int_t \int_\Omega \sigma \varepsilon (T_{amb}^4 - T^4) \quad (6)$$

the discrete energy balance for the external surfaces of the sample is obtained, given by:

$$\begin{aligned} \frac{k}{\Delta x/2} (T_{(i+1,j,k)} - T_{(i,j,k)}) &= h_{conv}(T_{amb} - T_{(i,j,k)}) \Delta y \Delta z + \sigma \varepsilon (T_{amb}^4 \\ &- T_{(i,j,k)}^4) \Delta y \Delta z \end{aligned} \quad (7)$$

As shown in Eq. (7), the natural convection heat transfer coefficient must be calculated in order to quantify the amount of thermal energy transferred to the external environment by the sample surfaces. Thus, for the lateral surfaces of the sample (4 surfaces in a vertical position), the convection coefficient h_{lat} is given by Eq. (8):

$$\bar{h}_{lat} = \frac{k}{H} \bar{Nu}_H \quad (8)$$

being Nu_H the Nusselt number based on H , which is obtained by the expression [12]:

$$\bar{Nu}_H = 0.68 + \frac{Ra_H^{1/4}}{[1 + (0.492/Pr)^{9/16}]^{4/9}} \quad (9)$$

In Eq. (9), Ra_H is the Rayleigh number based on H , defined by:

$$Ra_H = \frac{g \beta (T_s - T_{ar}) H^3}{\alpha \nu}, \quad (10)$$

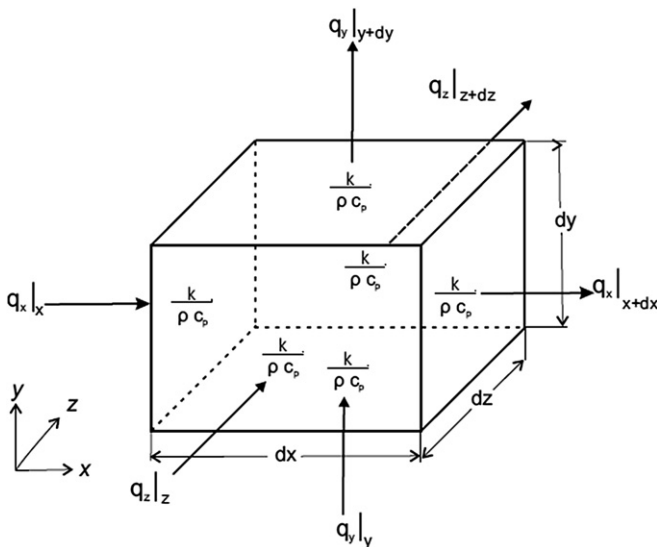


Fig. 2. Energy balance for an elemental volume.

where T_s and T_{ar} represent the temperature of the sample surface and the air, respectively. In this model, the air and the external environment are considered to be at the same temperature. The Prandtl number is given by Eq. (11).

$$\text{Pr} = \frac{\nu}{\alpha} \quad (11)$$

In Eqs. (8) to (11), k represents the thermal conductivity of the air; α and ν the thermal and momentum diffusivities respectively and β the thermal expansion coefficient. For the upper surface of the sample, the convection coefficient h_{sup} is defined by Eq. (12):

$$\bar{h}_{sup} = 0.15 \frac{k}{A_s/P} \bar{Ra}_L^{1/3} \quad (12)$$

Finally, for the lower surface the convection coefficient h_{low} is calculated by Eq. (13):

$$\bar{h}_{low} = 0.27 \frac{k}{A_s/P} \bar{Ra}_L^{1/4} \quad (13)$$

In Eqs. (12) and (13), A_s/P is the characteristic length defined as the relation between the area and the perimeter of the surface under consideration.

So far, a set of discrete energy balance equations have been developed which will be used to calculate the temperatures within the material and in its surfaces. Because of the explicit formation used as a temporal interpolation function, these sets of discrete equations can be solved individually. The Jacobi iterative method was used to develop a computational program called *TermoTest*® in order to calculate the temperature field during the cooling process imposed on the ceramic sample. The program was developed using the *MatLab*® platform and it provides the surface thermal map T_s of the material during the IR inspection, which will be later used to apply the inverse heat transfer problem.

3. The inverse problem for parameters identification

Information related to the thermal IR images collected during an NDT is widely used to extract quantitative information related to the subsurface defects present in the material being tested. This identification process can be performed through the Inverse Heat Transfer Problem, which uses the experimental thermal images for the determination of different parameters which play a role in the development of the thermal test. In this study the thermal maps collected experimentally were used to determine the thermal conductivity (k) and depth (y) of the defect present in the material. This quantitative information is obtained through the minimization of the following objective function:

$$J[k, y] \bar{k}, \bar{y} = \sum_{m=1}^M \int_{t_0}^{t_f} [Y_m(t) - T_s(x_m, t; \bar{k}, \bar{y})]^2 dt \quad (14)$$

In Eq. (14), $T_s(x_m, t)$ corresponds to the temperatures at position m , estimated by the solution of the direct problem, given in Section 2, while $Y_m(t)$ represents the temperatures obtained during the IR inspection; t_0 and t_f are the initial and final time of the experiment and M is the total number of measured positions. Given that in this work are considered three defective zones, $M = 3$. The task of the inverse heat transfer problem is to find the parameters (k and y) that minimize the difference between the theoretical and experimental results, using the Conjugate Gradient Method. This method consists of the selection of an appropriated search step size and direction of descent at each iteration in order to minimize the objective function, as described by Ozisik and Orlande [13]. The

direction of descent is obtained as a linear combination of the negative gradient direction at the current iteration and the direction of descent of the previous one. The complete iterative process of the Conjugate Gradient Method is presented in the next section.

3.1. The conjugate gradient method

The minimization iterative process requires the initial parameters, which will be used for the solution of the direct problem. Thus, the parameters that minimize the function given by Eq. (14) are determined by:

$$\begin{aligned} k^{p+1} &= k^p - \beta_k^p D_k^p \\ y^{p+1} &= y^p - \beta_y^p D_y^p \end{aligned} \quad (15)$$

In Eqs. (15), β^p and D^p are the search step size and the direction of descent, respectively, at the iteration p . As mentioned above, the direction of descent is a conjugation of the gradient direction, J^p , and the direction of descent of the previous iteration, D^{p-1} , given by:

$$\begin{aligned} D_k^p &= J_k^p - \gamma_k^p D_k^{p-1} \\ D_y^p &= J_y^p - \gamma_y^p D_y^{p-1} \end{aligned} \quad (16)$$

The conjugation coefficients γ^p are determined by the Fletcher-Reeves expression, given by:

$$\begin{aligned} \gamma_k^p &= \sum_{m=1}^M \int_{t=0}^{t_f} \frac{(J_k^p)^2}{(J_k^{p-1})^2} dt \\ \gamma_y^p &= \sum_{m=1}^M \int_{t=0}^{t_f} \frac{(J_y^p)^2}{(J_y^{p-1})^2} dt \end{aligned} \quad (17)$$

with $\gamma^p = 0$ for $p = 0$.

The gradient direction at iteration p , J^p , is obtained by differentiating Eq. (14) with respect to the unknown parameters k and y , resulting in:

$$\begin{aligned} J_k^p &= -2 \sum_{m=1}^M \int_{t=0}^{t_f} \frac{\partial T_s(x_m, t)^p}{\partial k} [Y_m(t) - T_s(x_m, t; k^p)] dt \\ J_y^p &= -2 \sum_{m=1}^M \int_{t=0}^{t_f} \frac{\partial T_s(x_m, t)^p}{\partial y} [Y_m(t) - T_s(x_m, t; y^p)] dt \end{aligned} \quad (18)$$

The derivatives which appear in Eqs. (18) are the *sensitivity matrix* or *Jacobian*, whose elements are called the *sensitivity coefficients*, defined as a measure of the sensitivity of the estimated temperature $[T_s(x_m, t)]$ with respect to changes in the parameters being estimated. In inverse heat transfer problems, it is desirable to have *linearly-independent sensitivity coefficients with large magnitudes* (large changes in the temperature due to small perturbations in the parameters), and thus the inverse problem is not very sensitivity to measurement errors and accurate estimates of the parameters can be obtained. The sensitivity coefficients,

$$\begin{aligned} J_k &= \sum_{m=1}^M \frac{\partial T_s(x_m, t)}{\partial k} \\ J_y &= \sum_{m=1}^M \frac{\partial T_s(x_m, t)}{\partial y} \end{aligned} \quad (19)$$

can be calculated using finite difference approximation. The numerical approximation of each of the partial derivatives present in Eqs. (19), results in:

$$\begin{aligned}\frac{\partial T_s}{\partial k} &= \frac{T_s(k + \Delta k) - T_s(k)}{\Delta k} \\ \frac{\partial T_s}{\partial y} &= \frac{T_s(y + \Delta y) - T_s(y)}{\Delta y}\end{aligned}\quad (20)$$

In Eqs. (20), Δk and Δy represent the perturbations applied to the thermal conductivity and defect depth, respectively. Finally, the search step size β^p that appears in Eqs. (15) is calculated by minimizing the function J^{p+1} with respect to β^p , resulting in:

$$\begin{aligned}\beta_k^p &= \sum_{m=1}^M \int_{t=0}^{t_f} \frac{[Y_m - T_s(x_m, t)] [J_k]^T D_k^p}{\{[J_k]^T D_k^p\}^2} dt \\ \beta_y^p &= \sum_{m=1}^M \int_{t=0}^{t_f} \frac{[Y_m - T_s(x_m, t)] [J_y]^T D_y^p}{\{[J_y]^T D_y^p\}^2} dt\end{aligned}\quad (21)$$

Once the Sensitivity Matrix J^p , the gradient direction J^p , the conjugation coefficient γ^p and the search step size β^p , have been calculated, the iterative procedure given by Eqs. (15) is implemented until a stopping criterion based on the *discrepancy principle* is satisfied. This principle states that the iterative procedure is stopped when the following criterion is satisfied:

$$J^{p+1} < \varepsilon \quad (22)$$

where the value of the tolerance ε is chosen so that sufficiently stable solutions are obtained. In this case, the iterative procedure is *stopped* when the residuals between measured and estimated temperatures are of the same order of magnitude as the measurement errors. Thus,

$$|Y_m(t) - T_s(x_m; t)| \approx \sigma_m \quad (23)$$

where σ^m is the standard deviation of the measurement error at each instant t , which is considered to be constant. Substituting Eq. (23) into Eq. (14), we obtain the value of the tolerance ε which is given by:

$$\varepsilon = \sum_{m=1}^M \sigma_m t_f \quad (24)$$

Thus, the stopping criterion is given by Eq. (22) with ε determined from Eq. (24).

3.2. Methodology and computational procedure for the estimation of defect depth and thermal conductivity

Fig. (3) shows the methodology implemented in this study for the re-construction of the IR image using the estimated depth and thermal conductivity of the defects in the material. The whole process begins with the infrared inspection of the ceramic sample. An infrared *Thermocam SC500* camera was used in experiments and the frame rate acquisition was of 1 image/s. The ambient conditions under which the experiment was carried out were monitored for later use in the numerical simulation. Information concerning to dimensions of the test sample and its defects are also used as input data in the simulation program.

A preliminary analysis with the computational algorithm is conducted in order to estimate the detectability level as a function of the initial temperature; this is, the temperature at which the sample leaves the furnace and the cooling process is imposed. This

analysis is essential in order to better select the defective zone once the thermogram sequence has been collected with the infrared camera. Once the initial temperature T_o is established, both the experimental test and numerical simulation are carried out using the real parameters in the computation code, i.e., sample and defect dimensions, ambient temperature and thermophysical properties of the material.

The experimental and simulated thermogram sequences are collected from which the temperature evolution curves of defective areas will be extracted. These curves in the form of column vectors $[T_s(x_m; t)]$ and $Y_m(t)$ are used in the implementation of the inverse heat transfer method which requires the minimization of the objective function [Eq. (14)] using the CGM. The main steps of the minimization computational procedure are explained as follows:

- Step 1 Compute the sensitivity coefficients J^p defined by Eq. (19), using the numerical approximation given in Eq. (20) and the gradient direction J^p from Eq. (18).
- Step 2 Compute the conjugation coefficients γ^p defined by Eq. (17) and the direction of descent D^p given by Eq. (16).
- Step 3 With a knowledge of J^p , $Y_m(t)$, $T_s(x_m; t)$ and D^p , calculate the search step size β_k^p from Eq. (21). With the initial parameters k^p and y^p , and the knowledge of β_k^p and D^p , calculate the new estimated parameters k^{p+1} and y^{p+1} using Eq. (15).
- Step 4 Replace p by $p+1$ and solve the direct problem (Thermal NDT Model) in order to obtain the temperature evolution map $T_s(i, k, t)$ (Section 2) using the computational algorithm *TermoTest*[®].
- Step 5 Check the stopping criterion given by Eq. (22). If it is not satisfied, return to Step 1.

4. Results and discussions

The main objective of this study was to validate the application of the inverse heat transfer problem to estimate the thermal conductivity and depth of subsurface defects during the inspection of ceramic bricks by infrared thermography. Numerical simulations were conducted through the solution of the direct problem detailed in Section 2 in order to obtain the estimated evolution temperature $T_s(x_m, t)$ of the defective area, which together with the experimental results will lead to the determination of the above-mentioned defect properties.

The thermophysical properties of the inspected material and the defects are presented in Table 1. For the defect type, the air at $T=298.15$ K was considered. Table 2 shows the natural convection heat transfer coefficients calculated for each of the surfaces of the material, considering $T_{ar}=298.15$ K and $T_s=523$ K.

All the numerical simulations presented in this study were carried out using a mesh with $N_x=52 \times N_y=26 \times N_z=20$ number of elements and a time step of $\Delta t = 0.06$ s, ensuring the convergence of the solution and consistency of the results.

4.1. Impact of the initial temperature on defects detectability

The first parameter analyzed is the detectability level of the defects as a function of the initial cooling temperature T_o . The main objective of the analysis is to study quantitatively under which conditions the defects present the greatest thermal contrast (defined as the temperature difference between defective and non-defective areas), considering air defects at different depths. It is important to remember that the initial cooling temperature is the temperature at which the sample leaves the furnace, after which the cooling process then begins. Figs. (4) to (6) show the evolution of the thermal contrast during the cooling process for defects

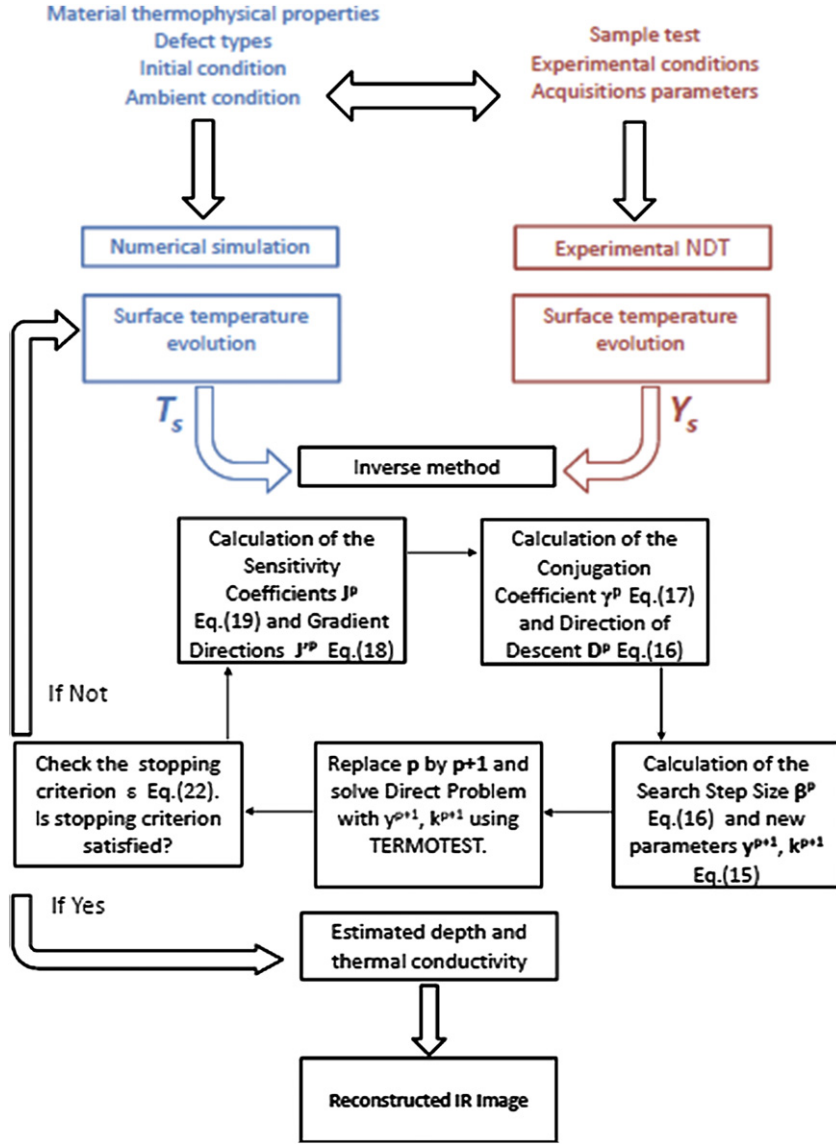


Fig. 3. Implemented methodology for the estimation of defect depth and thermal conductivity.

Table 1

Thermophysical properties of material and defects used in the numerical simulation.

Thermophysical property	Bulk material [14]	Defects, considering air at $T = 298.15$ K
k (W/m K)	1.0	0.0263
ρ (kg/m ³)	1900	1.1614
c_p (J/kg K)	1000	1007
ϵ	0.93	—

located at 7.5 mm, 12.0 mm and 14.0 mm, respectively, for three different initial temperatures: 423 K, 473 K and 573 K.

It is important to note from these results that the higher the initial cooling temperature T_0 , the higher the thermal contrast of the detected defects. From Fig. (4) it can be observed that for the defect with 7.5 mm depth, it is possible to increase the thermal

Table 2

Surface heat transfer coefficients for natural convection.

Initial temperature T_0 (K)	\bar{h}_{lat} (W/m ² K)	\bar{h}_{upp} (W/m ² K)	\bar{h}_{low} (W/m ² K)
423	9.6	5.1	10.4
473	10.2	5.5	11.0
523	10.7	5.8	11.6

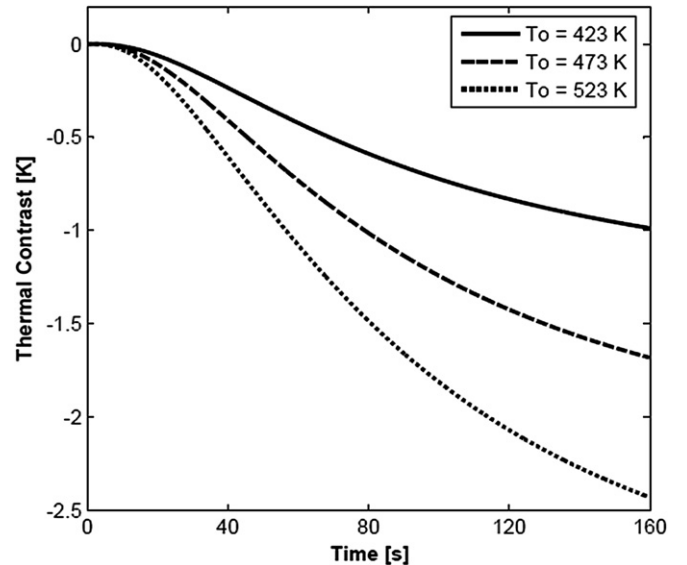


Fig. 4. Thermal contrast evolution curves for different initial temperatures, considering an air defect located at $y = 7.5$ mm, $\varnothing = 4.5$ mm and $T_{amb} = 298$ K.

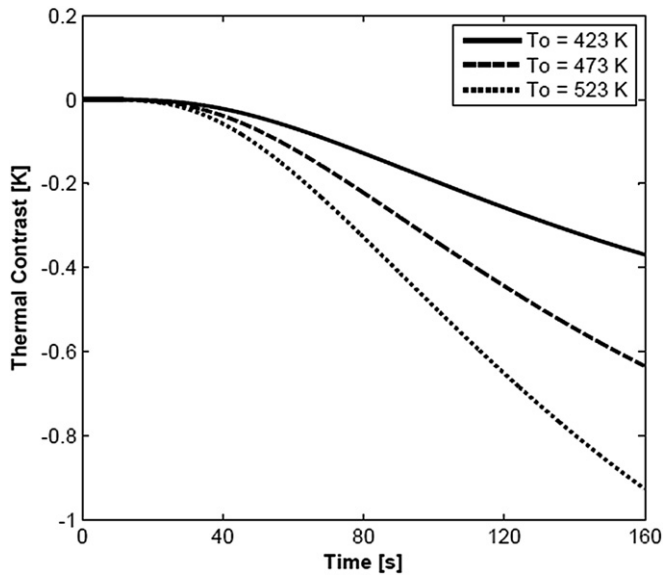


Fig. 5. Thermal contrast evolution curves for different initial temperatures, considering air defect located at $y = 12.0$ mm, $\varnothing = 4.5$ mm and $T_{amb} = 298$ K.

contrast from 1.0 K to 2.4 K with an initial cooling temperature of 423 K. For the defect located at 12.0 mm depth [see Fig. (5)], it is observed that despite an increase in the detectability level, the length scale of the obtained thermal contrast is significantly smaller than in the previous case. A similar result was obtained for the defect at 14.0 mm depth, with an increase in the thermal contrast of 0.18 K when an initial cooling temperature of 523 K was imposed.

From these results it can be concluded that the highest level of detectability of the defect is achieved by imposing an initial cooling temperature of 523 K and the occurrence of the maximum thermal contrast takes place at 160 s from the beginning of the cooling process. This situation is illustrated in Figs. (7) to (9), showing three different thermal images obtained by numerical simulation, each representing the thermogram of maximum thermal contrast achieved when three different initial cooling temperature are used:

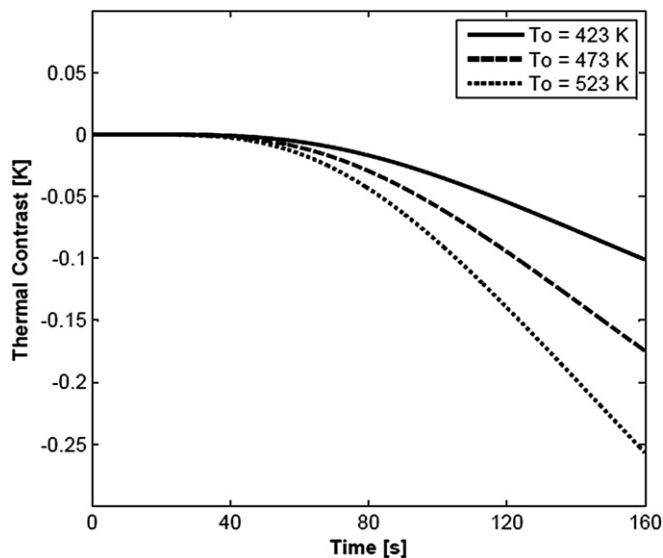


Fig. 6. Thermal contrast evolution curves for different initial temperatures, considering air defect located at $y = 14.0$ mm, $\varnothing = 4.5$ mm and $T_{amb} = 298$ K.

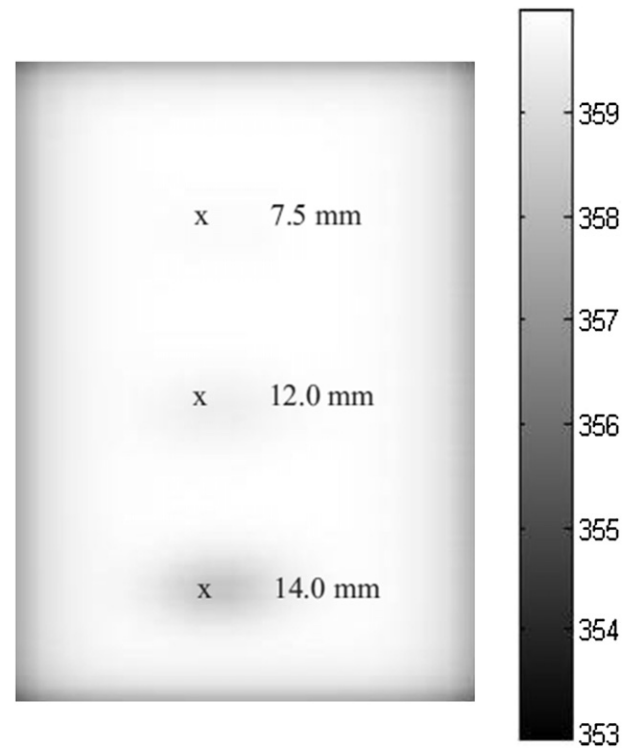


Fig. 7. Thermal images obtained by numerical simulation, considering $T_o = 323$ K.

423 K, 473 K and 523 K. It can be observed that all three defects can be clearly detected when the initial cooling temperature is 523 K.

4.2. Thermal sensitivity analysis

The process of identifying the parameters associated with the internal defects present in the material (thermal conductivity and

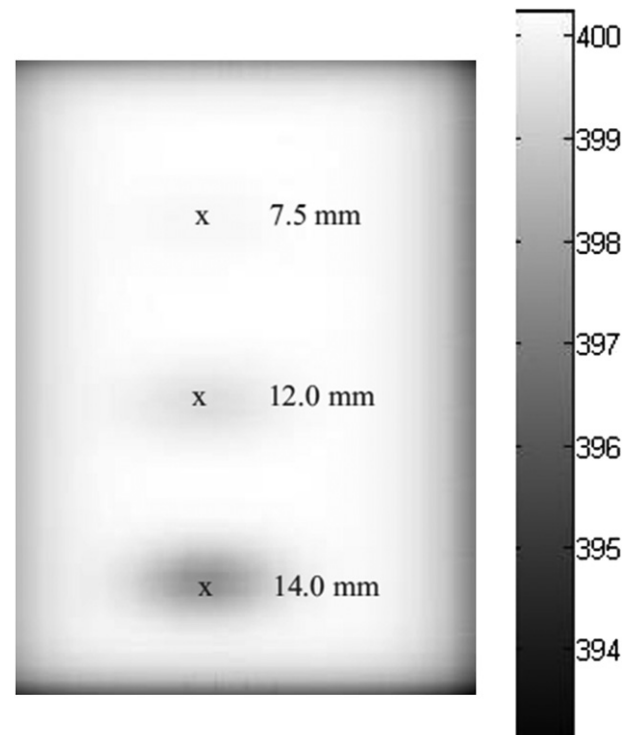


Fig. 8. Thermal images obtained by numerical simulation, considering $T_o = 423$ K.

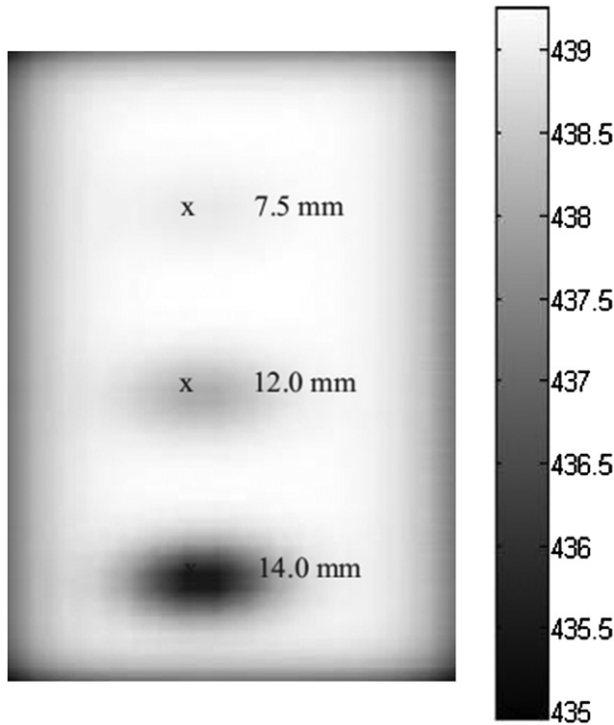


Fig. 9. Thermal images obtained by numerical simulation, considering $T_0 = 473$ K.

depth) requires a sensitivity analysis of the thermal model in relation to these properties. Through this analysis it is possible to observe the response in terms of the estimated temperature (by numerical simulation) when a perturbation is applied to each parameter. The results of the sensitivity analysis give an indication of the best measuring location and times to be used in the inverse problem, which corresponds to linearly-dependent sensitivity coefficients with large magnitudes.

In Figs. (10) and (11) the sensitivity coefficients are plotted for the defect depth and thermal conductivity, respectively. These coefficients were calculated using the numerical approximation

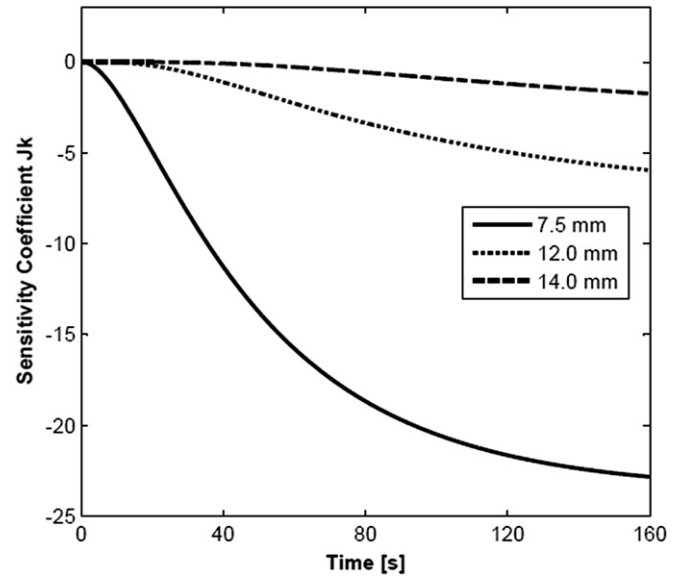


Fig. 11. Sensitivity coefficient of the thermal conductivity.

given by Eqs. (19). The perturbation applied to each of the parameters was $\Delta = 1e^{-5}$. These results reveal that the defect located at 7.5 mm is the most sensitive to the perturbation applied to the depth and thermal conductivity, followed by the defects located at 12.0 mm and 14.0 mm.

It can also be seen from the coefficients that the depth of the defects is the parameter that has most significant effect on the temperature of the defective area. Once again, when the defect is located closer to the surface the temperature becomes more sensitive to the perturbations applied to each parameter.

4.3. Inverse heat transfer results

Figs. (12) to (14) show a comparison between the temperature curves of the defective areas obtained by numerical simulation using the initial guess parameters ($T_{\text{numerical}}$), the estimated

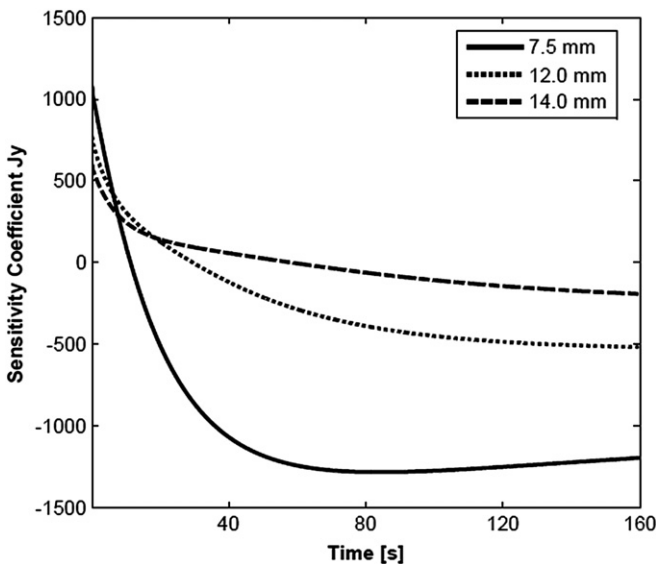


Fig. 10. Sensitivity coefficients of the defect depth.

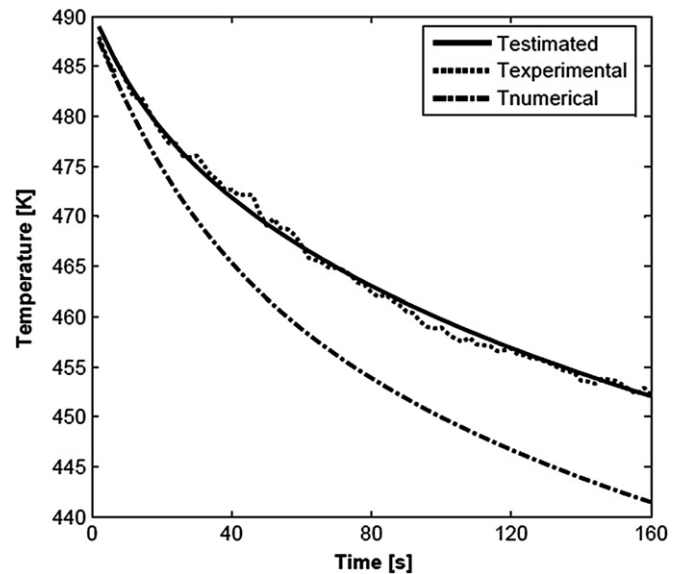


Fig. 12. Comparison of the experimental, simulated and estimated temperature evolution curves for defect located at $y = 7.5$ mm.

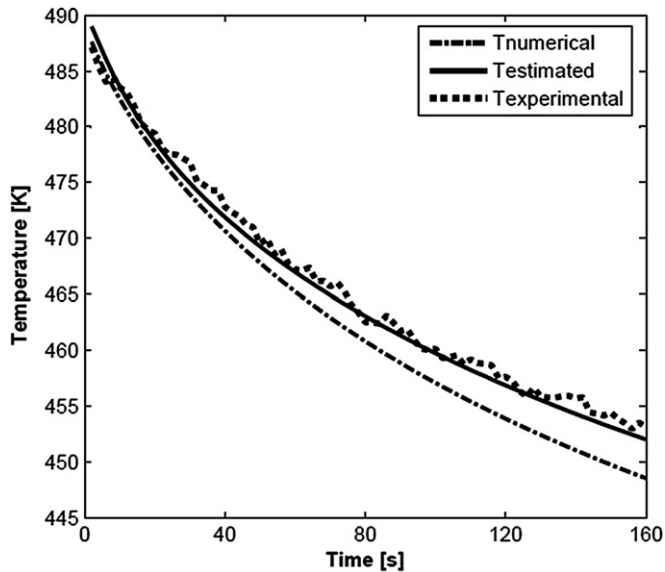


Fig. 13. Comparison of the experimental, simulated and estimated temperature evolution curves for defect located at $y = 12.0$ mm.

temperature using the new thermal conductivity and the depth when applying the inverse problem ($T_{estimated}$), and the temperature curves acquired from the surface investigated during a real non-destructive test by IRT ($T_{experimental}$). The three figures correspond to defects located at 7.5 mm, 12.0 mm and 14.0 mm from the surface, respectively.

As expected, the best approximation of the estimated curve was that corresponding to the defect at 7.0 mm, followed by the estimated curves of the defect at 12.0 mm and 14.0 mm. The approximation of the curves was considerably affected by the behavior of the sensitivity coefficients and also because of the experimental measurement uncertainties; as the defects become closer to the surface of the material, the accuracy of the estimation of the properties considered are better.

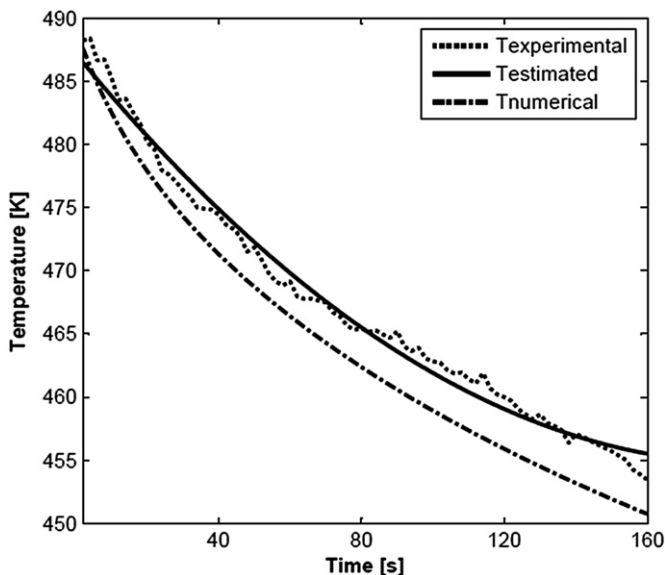


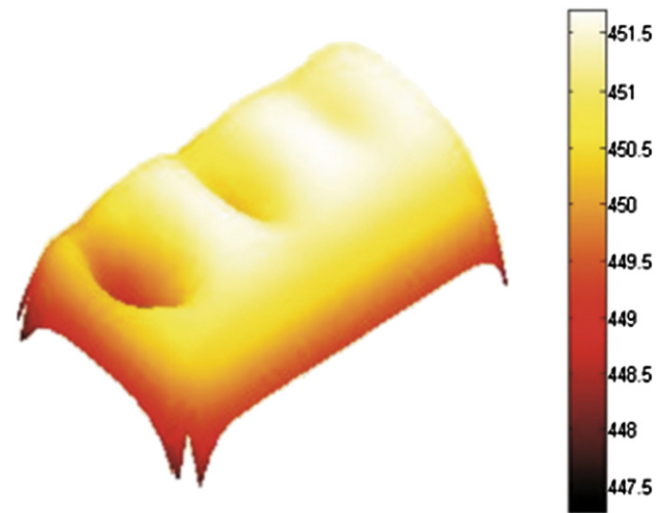
Fig. 14. Comparison of the experimental, simulated and estimated temperature evolution curves for defect located at $y = 14.0$ mm.

Table 3

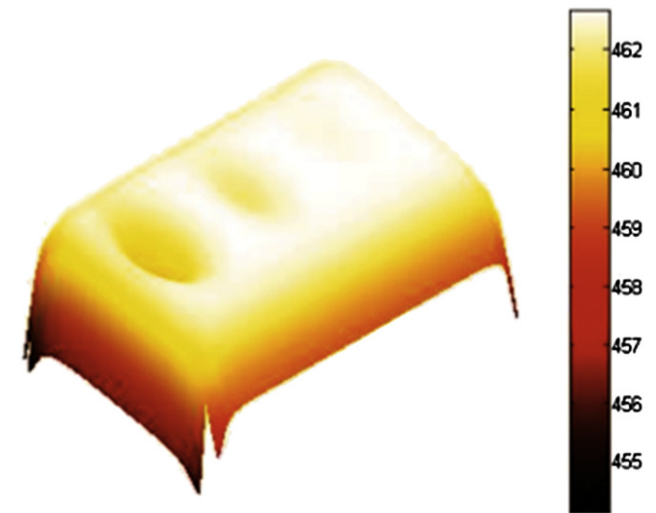
Measurement uncertainties and relation between the initial parameters used in the thermal simulation and the estimated applying the inverse heat transfer method.

Defect	$U(\bar{q})$	$k_{initial}$	$k_{estimated}$	$z_{initial}$	$z_{estimated}$
Depth (mm)	(K)	(W/m K)	(W/m K)	(mm)	(mm)
7.5	6.64	0.0263	0.0392	7.5	7.9
12.0	7.87	0.0263	0.0437	12.0	12.8
14.0	8.62	0.0263	0.0695	14.0	15.3

Table 3 shows the experimental measurement uncertainties $U(q)$ and the relation between the initial parameters used in the numerical simulation and the estimated values obtained through the application of the inverse heat transfer method. As can be



a 1st iteration - initial guess



b 2nd iteration - reconstructed IR image

Fig. 15. Comparisons between the thermal map obtained from the numerical results [Fig. 15(a)] and the reconstructed IR image obtained using the new thermal conductivity and defect depth [Fig. 15(a)]. Both images correspond to 160 s after the beginning of the cooling process.

observed, the largest errors in the estimated properties correspond to the thermal conductivity which, once again, agrees with the behavior of the sensitivity coefficient of that parameter. Another important feature revealed by the results is that as the defect becomes farther from the inspected surface, the magnitude of the thermal conductivity becomes larger, which agrees to the physical phenomena of the thermal process: a deeper defect transfers less thermal energy to the external environment thus producing an increase in the temperature of the internal air which, in turn, increases the thermal conductivity. Regarding the estimated depth, it can be clearly observed that the estimation was quite closed to the initial guess, which is also consistent with the high sensitivity coefficient of that property.

Finally, Fig. 15 shows two different thermal images, both corresponding to 160 s after the beginning of the imposed cooling process. Fig. 15(a) was obtained by numerical simulation using the initial guess parameters, while Fig. 15(b) is the reconstructed image when the new thermal conductivity and depth obtained in the inverse method were used. *IrView*[®] [15] was employed to enhance the visibility of the images.

The effect of the estimated properties on the thermal pattern of the inspected surface can be observed from these images. In the first iteration the defects exhibit greater thermal contrast than in the reconstructed image. This is because of the influence of the estimated depth on the thermal behavior of the defective areas. Despite the increase in the value of the estimated thermal conductivity, the defect depth is the property that most affects the thermal pattern of the infrared images, as demonstrated in the sensitivity analysis.

5. Concluding remarks

The conjugate gradient method was successfully applied in the determination of the thermal conductivity and depth of defects present in ceramic materials using data obtained through the solution of a thermal model and from experimental results. The inspection method proposed herein is based on a study of the thermal behavior of the sample test during the imposition of a cooling regime process. The thermal model developed allows the detectability of internal defects to be investigated as a function of the initial cooling temperature, indicating that at higher initial temperatures the defects present greater thermal contrast.

The sensitivity analysis developed in this study revealed that the defect depth is the parameter with the greatest influence on the thermal pattern of the defective areas. The infrared image reconstructed using the parameters estimated using the inverse heat transfer problem presented good agreement with the physical interpretation of the inspection method.

Acknowledgements

The authors are grateful for the financial support of CNPq as well as the international student program PEC-PG both awarded by the Brazilian Federal Government.

References

- [1] X. Maldague, *Theory and Practice of Infrared Technology for Nondestructive Testing*. John Wiley & Sons, New York, 2001.
- [2] F.S. Magnani, R.N. Tavares da Silva, Infrared thermography applied to quantitative determination of spatial and thermophysical parameters of hidden included objects, *Appl. Thermal Eng.* 27 (2007) 2378–2384.
- [3] E. Barreira, V.P. de Freitas, Evaluation of building materials using infrared thermography, *Constr. Build. Mater.* 21 (2007) 218–224.
- [4] I.C. Guerrero, S.M. Ocaa, I.G. Requena, Thermal-physical aspects of materials used for the construction of rural buildings in Soria (Spain), *Constr. Build. Mater.* 19 (2005) 197–211.
- [5] B. Sawaf, M.N. Ozisik, An inverse analysis to estimate linearly temperature dependent thermal conductivity components and heat capacity of an orthotropic medium, *Int. J. Heat Mass Transfer* 38 (1995) 3005–3010.
- [6] Ch. H. Huang, J. Yan, An inverse problem in simultaneously measuring temperature-dependent thermal conductivity and heat capacity, *Int. J. Heat Mass Transfer* 38 (1995) 3433–3441.
- [7] Ch. H. Huang, S.C. Chin, A two-dimensional inverse problem in imaging the thermal conductivity of a non-homogeneous medium, *Int. J. Heat Mass Transfer* 43 (2000) 4061–4071.
- [8] M.H. Chang, C.H. Cheng, Nondestructive inverse method for determination of irregular internal temperature distribution in PEMFCs, *J. Power Sources* 142 (2005) 200–210.
- [9] M. Hanke, *Conjugate Gradient Type Methods for Ill-Posed Problems*. John Wiley & Sons, New York, 1995.
- [10] C.H. Cheng, C.Y. Wu, An approach combining body-fitted grid generation and conjugate gradient methods for shape design in heat conduction problems, *Numer. Heat Transfer, Part B* 77 (2000) 69–83.
- [11] C.R. Maliska, *Transferência de Calor e Mecânica dos Fluidos Computacional*, LTC. Livros Técnicos e Científicos Editora S.A., Rio de Janeiro, 2004.
- [12] S.W. Churchill, H.S. Chu, Correlating equations for laminar and turbulent free convection from vertical at plate, *Int. J. Heat Mass Transfer* 18 (11) (1975) 1323–1329.
- [13] N. Ozisik, H.B. Orlande, *Inverse Heat Transfer: Fundamentals and Applications*. Taylor and Francis, NY, 2000.
- [14] E. Facincani, *Tecnologia Ceramica: I Laterizi*. Faenza, Italia, 1992.
- [15] M. Pilla, M. Klein, *IrView V.1.7.5*. Free Software Foundation Inc., 2008.